ACS OMEGA

Open Access

http://pubs.acs.org/journal/acsodf

Article

High-Frequency AC Heating Strategy of Electric Vehicle Power Battery Pack in Low-Temperature Environment

Wei Cui, Yuan Li,* Ze-yu Ma, Jing-xuan Nie, and Yu-chen Liu

Cite This: *ACS Omega* 2024, 9, 12753−12767

Read Online

ACCESS | Metrics & More | Article Recommendations

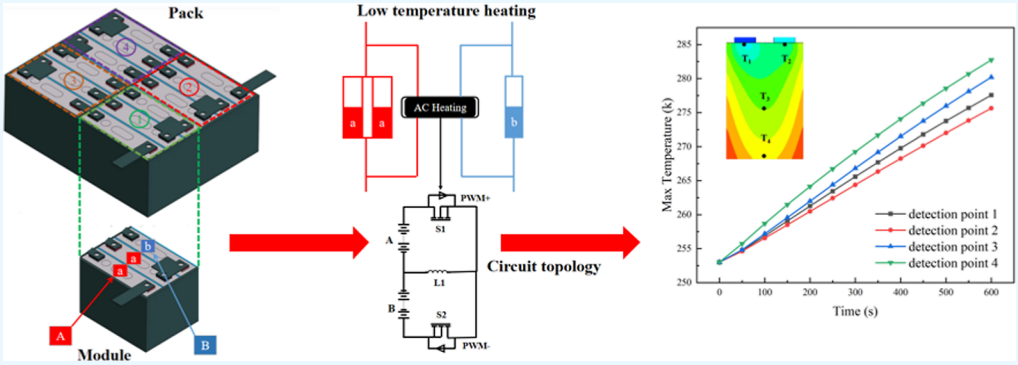

ABSTRACT: In this paper, a heating strategy using high-frequency alternating current (AC) is proposed to internally heat lithium-ion batteries (LIB) at low temperatures. The strategy aims to strike a good balance between rapid heating of the battery at low temperatures and minimizing damage to the battery's lifespan without the need for an additional power source. The strategy presents an electrochemical−thermal coupling model to simulate and predict the temperature rise and temperature distribution of a 50 A h $LiFePO_4$ square battery at different C-rates, the effect of high-frequency AC on battery life, and the validity of the model as verified by experiments. The experimental and simulation results show that this strategy can achieve faster heating speeds and better temperature consistency without affecting battery life. The best heating effect can be achieved at a frequency of 500 Hz (4.2C), and the temperature of the battery rises from 253.15 to 278.15 K within 365 s, for an average heating rate of 3.29 K/min. Researching low-temperature AC heating methods has important value for energy conservation because it can improve heating efficiency, expand application areas, promote technological innovation, and enhance product quality.

1. INTRODUCTION

In recent years, there has been booming social and economic development, accompanied by increasing global environmental problems and growing global energy demand. The main energy in electric vehicles comes from batteries, under the background of protecting the environment and saving energy.[1] Electric vehicles (EV) are vigorously developing worldwide.[2] LIBs are often used in automobile power batteries because of their long life, environmental protection, low self-discharge rate, high durability, and high energy density.[3] In AC excitation heating, the C rate is defined as the rate of charging or discharging of the battery, usually expressed as a multiple of the battery capacity. For example, a 1C charging or discharging rate means operating with a current equal to the battery capacity. The definition of C-rate remains the ratio of current to battery capacity.[4] However, the performance of LIB is obviously affected by temperature, particularly below 253.15 K.[5] In a low temperature environment, the diffusion rate of solid lithium decreases, the conductivity of the electrolyte decreases, and the charge transfer resistance on the electrode surface increases.[6] The battery capacity and battery characteristics are seriously attenuated,[7] leads to some problems such as internal resistance increasing and endurance decreasing.[8] In addition, with the decrease of temperature, the battery performance will be degraded.[9] Therefore, the preheating of power batteries has become an inevitable demand, and it is very urgent to find a suitable preheating method.[10]

The battery heating process is also included in the battery thermal management system. The best battery heating design must meet two goals: heating the battery in the shortest time possible and maintaining the temperature uniformity of the battery.[11] The maximum temperature difference between batteries cannot exceed 5 K.[12] Nowadays, battery preheating

Received: October 28, 2023
Revised: February 21, 2024
Accepted: February 27, 2024
Published: March 11, 2024

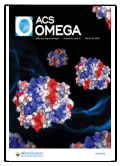

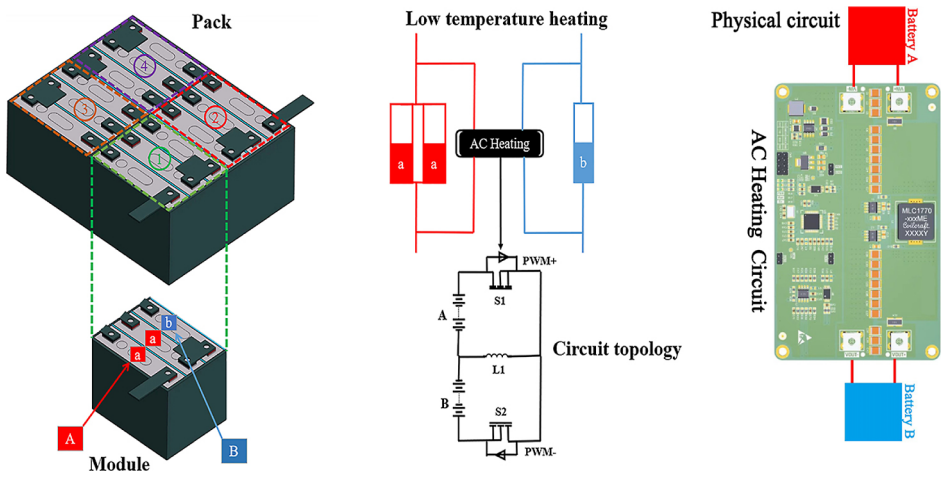

Figure 1. AB heating strategy diagram of the AC heater for a battery pack.

methods are mainly divided into external heating and internal heating.[13] External heating usually uses air or liquid as the medium to heat the battery: the heat transfer phase change material is wrapped outside the battery.[14−16] External heating will lead to heat diffusion, resulting in uneven battery heating.[17] The external heating device has the disadvantages of large volume, high cost, large energy loss, and uneven heating. Similarly, the internal heating can be divided into direct current (DC) and alternating current (AC).[18] When charging or discharging, the battery is heated by using the real part of its own impedance, the internal heating mode does not use an external heater, which eliminates the heat lost by heat conduction and prevents the heat from spreading to the environment.[19] Furthermore, the DC heating method heats up quickly, but it can cause lithium deposition, which affects the battery.[20,21] By comparison, the AC heating mode heats the battery by transferring energy within the battery packs. The AC heating method effectively prevents lithium deposition during heating and avoids reducing the state of charge (SOC) and state-of-health (SOH).[22] It offers better heating efficiency, temperature uniformity, and more potential for further development.

Cai et al.[23] proposed a self-heating strategy without an external power supply based on bidirectional pulsed current. The electro-thermal coupling model of LIB is built, and the LIB can be warmed up from 263.15 to 273.15 K in about 120 s. Zhang et al.[24] proposed an AC heater based on switched capacitors for heating two 18650-type lithium ternary batteries. At the optimal heating frequency of 10 kHz, the battery can be heated from 253.15 to 273.15 K in 2.2 min, consuming only 5.4% of the battery energy. However, the article does not provide an in-depth analysis and discussion of the effect of heating methods on battery life. Zhang et al.[25] used sinusoidal AC to heat LIB. They simulated the battery using an equivalent circuit model and heated it from 253.15 to 278.15 K within 15 min. The temperature distribution is uniform, but the equivalent circuit model cannot accurately reflect the electrochemical and thermodynamic processes of the battery. Hu et al.[26] designed a self-heating circuit to preheat the battery using an AC with controllable frequency and amplitude. The battery is heated from 253.15 to 278.15 K within 15 min, which has an average temperature rise rate of 1.67 K/min. Jiang et al.[27] designed a soft switching circuit to warm a battery pack from 252.35 to 275.25 K within 600 s. They simulated the process using equivalent circuit models and analyzed the internal thermal reaction of the battery pack. However, these models have a relatively low accuracy and cannot accurately reflect the complex heat distribution inside the battery. Shang et al.[28] designed an AC electric heating circuit without external power supply equipment. They used a MOSFET switch in circuit control. By using 833 Hz high-frequency AC with an amplitude of 3.1C, it took 5.9 min to heat a lithium battery from 253.15 to 273.15 K, consuming about 5% of the energy. This proves that the energy generated by mutual excitation within batteries is used for heating. Shang et al.[19] conducted simulations based on the experiments established, an electrochemical-thermal coupling model consider high-frequency AC heating. The model was verified by experiments at different heating frequencies and effective values. When the switching frequency increased to 45 kHz, the heating time of the battery from 253.1 to 273.15 K was 7.4 min, and the rising rate of temperature reached 2.70 K/min. Increasing the AC may lead to Li-ion deposition and battery life reduction; they did not consider the effect of AC heating on lithium deposition in LIB. The results showed that the temperature performance of the battery can be improved by using the AC heating strategy. Although relevant studies indicate the AC heating method's superiority compared to other heating methods, model simulations cannot accurately reflect the influence of internal heat distribution and alternating current on battery life. The main challenge in battery heating is accurately simulating and predicting the heat distribution inside the battery.

However, there is little literature on the model simulation to accurately reflect the internal heat distribution of the battery and the impact of the AC device on the battery life. In this study, a high-frequency AC heater for batteries is designed, and the design consists of a MOSFET and inductor. By using complementary pulse width modulation (PWM) signals, the MOSFET switch generates high-frequency AC for heating batteries. The switching frequency of the MOSFET is controlled to regulate the preheating speed. Based on the AC heating device, an electrochemical coupling model is developed to simulate and predict the effects of different C-rates on battery temperature rise, voltage, temperature distribution, and battery life. The validity of the model is verified by experiments. In summary, the heating strategy offers advantages such as uniform heat generation, fast heating speed, simple control, low cost, and independence from battery shape. Using high-frequency AC to charge or discharge LIB can effectively address the issue of battery aging due to voltage imbalances. The AC heating

https://doi.org/10.1021/acsomega.3c08522
ACS Omega 2024, 9, 12753−12767

strategy provides a feasible solution for rapidly heating lithium batteries at low temperatures, which is particularly significant for promoting and advancing electric vehicle adoption in cold regions.

2. AC HEATING CIRCUIT DESIGN AND ELECTROCHEMICAL−THERMAL MODEL DESCRIPTION

2.1. AC Heating Circuit Design Model. The paper proposes a power battery low-temperature AC preheating circuit to enhance battery performance at low temperatures. The heating device is used in the LIB pack of the electric vehicle. Figure 1 shows that the LIB pack consists of four modules; each module is divided into AB batteries. The designed circuit is connected to both ends of batteries A and B to facilitate quick preheating of the AB batteries. Battery A consists of $n + 1$ cells (a) connected in series, while battery B consists of n cells (b) connected in series. The number of batteries in battery A is greater than the number of batteries in battery B. The difference in battery count allows for the formation of a potential difference within the battery module. Consequently, the direction and magnitude of the current can be accurately adjusted, realizing voltage elevation conversion. High-frequency AC is applied to alternately charge or discharge within the battery modules, effectively dividing the battery into two parts without the need for additional power supplies or components. The battery A, the inductor L_1, and the MOSFET tube S_1 are turned on, and S_2 is turned off, forming loop 1. And the battery B, inductor L_1, and MOSFET tube S_2 are turned on, and S_1 is turned off to form loop 2.

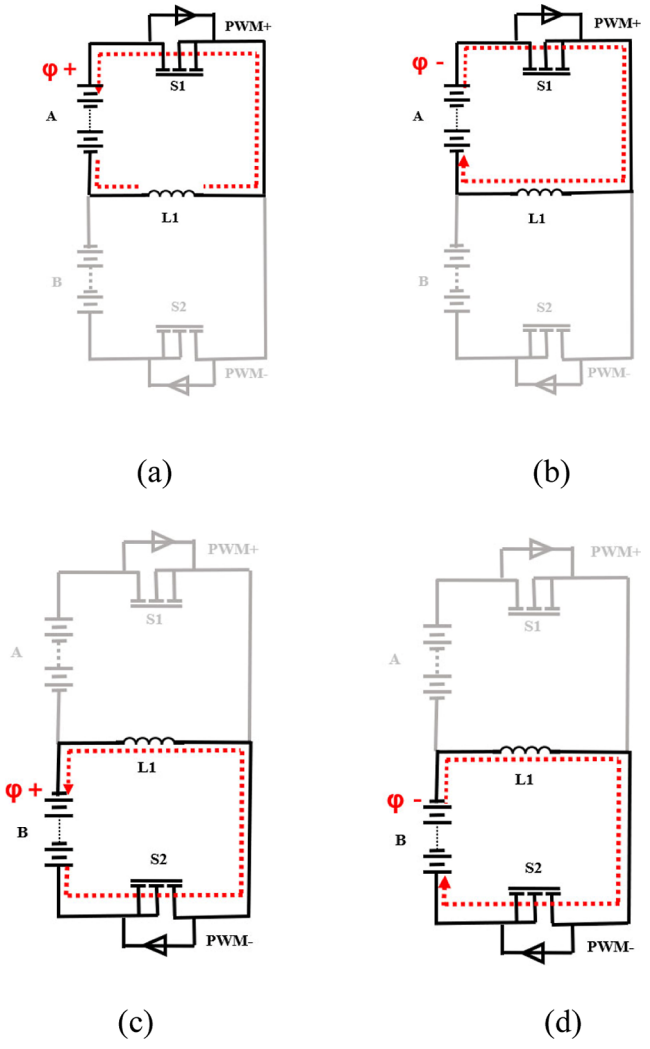

Figure 2. Operating mode of the AC heater for the AB battery pack: (a) mode I, (b) mode II, (c) mode III, and (d) mode IV.

The heating process is divided into two modes: the charging mode and the discharging mode. In mode I (Figure 2a), battery A is charged by inductor L_1, causing a decrease in inductor current I_L and an increase in potential at the end of battery A, resulting in battery A being charged. In mode II (Figure 2b), S_1 stays on and S_2 stays off. When the inductor current I_L drops to 0 at t_1, Mode II begins. Battery A transfers energy to inductor L_1, and then the inductor current I_L drops (rises reversely). The potential at the end of battery A drops, and battery A discharges. In mode III (Figure 2c), S_2 is on and S_1 is off, connecting inductor L_1 with battery B. The inductor current I_L linearly rises, causing an increase in the potential of battery B and initiating charging. In mode IV (Figure 2d), S_2 remains on and S_1 remains off until the inductor current I_L rises to 0. The potential of battery B drops. Mode IV begins. Inductor L_1 is charged by battery B, storing energy in the inductor.

Modes I and II involve AC charging and discharging of battery A, while Modes III and IV involve AC charging and discharging of battery B. During Modes II and III, energy is transferred from batteries A to B, while during Modes IV and I, energy is returned from batteries B to A to ensure thermal consistency within AB batteries.

2.2. P2D Electrochemical−Thermal Model. The P2D (pseudo-two-dimensional) model using porous electrodes is based on a physical model proposed by Newman.[29] The separation process of a lithium battery can be divided into a particle domain and an electrode domain. In the particle domain, the lithium conservation problem can be solved by Fick's law; the particles are usually considered to be spherical. In the electrode domain, the problems of charge conservation in solid phase and electrolyte and mass conservation in electrolyte have been solved.[30] The P2D model accurately captures Li-ion migration. Figure 3 shows the basic structure of a LIB. The electrolytic liquid phase flows continuously in the negative, separator, and positive electrodes, while the solid phase exists only in the negative and positive electrodes. During the discharge of lithium batteries, Li-ion will diffuse to the surface of negative particles and undergo an electrochemical reaction, releasing an electron and transferring lithium to the electrolyte phase. Li-ion diffuses and conducts through the electrolyte solution to the cathode, transferring lithium to the cathode solid phase; lithium is stored in the anode particles.[31] The change of electrolyte concentration will affect the migration rate of the Li ion in the battery. A series of equations, such as solid−liquid diffusion coefficient, Li-ion migration, and energy conversion, will be solved by simulation calculations at the level of the battery material.[32] The model can more accurately reflect the change and distribution of the reaction heat generated inside the battery.

2.3. Electrochemical Kinetics and Boundary Conditions. The P2D model mainly includes five main equations.[33] These equations are the conservation of lithium in the electrolyte phase, the conservation in the solid phase, the charge conservation in the solid phase, the charge conservation in the electrolyte phase, and the conservation of lithium in the

https://doi.org/10.1021/acsomega.3c08522
ACS Omega 2024, 9, 12753−12767

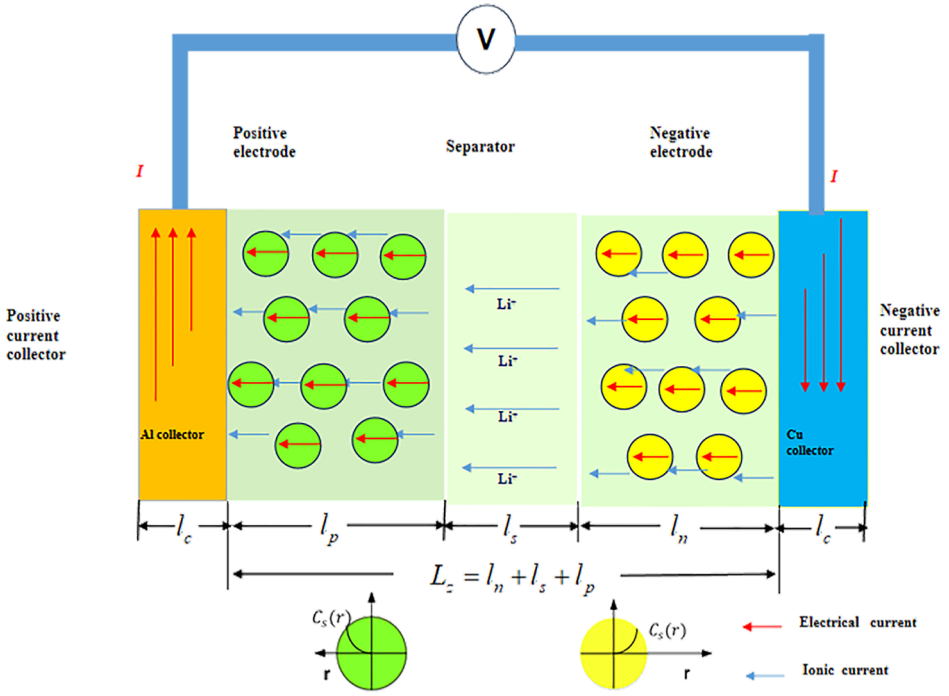

Figure 3. Schematic diagram of the P2D model LIB structure.

Table 1. Parameters Used in the P2D Model

parameter	negative electrode	separator	positive electrode	unit	ref
δ_i	100	52	183	μm	30
R_s	$2.5 \times 10^{-5}/2$		$1.6 \times 10^{-5}/2$	μm	30
ε_1	0.56		0.435		40
ε_2	0.3	0.4	0.28		40
C_0	2000	2000	2000	mol/m^3	30
C_1	3900		16,361	mol/m^3	41
$C_{1,max}$	26,390		31,540	mol/m^3	41
$\mathcal{T}_i$	0.357	1	0.444		30
$D_{s,i}$	3.9×10^{-14}		1×10^{-13}	m^2/s	30
$E_{d,i}$	2×10^4		8.6×10^4		30
δ_i	0.01		2		42
k	2.072818×10^{-11}		2.072818×10^{-11}	mol/m^2 s/(mol/m^3)$^{1.5}$	30
$E_{r,i}$	2×10^4		9×10^3		30
D_e		7.5×10^{-11}		m^2/s	30
t_+		0.363			40
α_a	0.5		0.5		40
α_c	0.5		0.5		40
γ	1.5	1.5	1.5		40
R		8.3143		C/mol	30
F		96,485		J/mol K	30

Table 2. Thermodynamic Parameters of Materials for Each Component of the Square Battery[44]

structure name	material	density (kg/m^3)	specific heat [J/(kg·K)]	thermal conductivity [W/(m·K)]
cell case	stainless steel	1080	1450	0.21
positive current collector	aluminum foil	2702	903	236
negative current collector	copper foil	8935	385	398
positive pole	LFP	2840	1200	3.91
negative pole	graphite	1671	1437	3.28
cell diaphragm	PP	658	1978	0.355

electrolyte phase. These equations describe the Butler−Volmer equation with boundary conditions.

2.3.1. Mass Conservation. In an active solid particle, the material balance of Li-ion is controlled by Fick's second law in spherical coordinates[34,35]

https://doi.org/10.1021/acsomega.3c08522
ACS Omega 2024, 9, 12753−12767

Table 3. Thermophysical Parameters of the Internal Composition of the Square Battery

structure name	density (kg/m^3)	specific heat [J/(kg·K)]	thermal conductivity [W/(m·K)]
cell core	300	1100	x:0.91; y:2.73 z:2.73
positive pole (Al)	2702	871	236
negative pole (Cu)	8935	381	398

$$\frac{\partial C_S}{\partial t} - \frac{D_s}{r^2}\frac{\partial}{\partial r}\left(r^2\frac{\partial C_S}{\partial r}\right) = 0 \tag{1}$$

with boundary conditions

$$D_s\left(\frac{\partial C_s}{\partial r}\right)_{r=0} = 0 \text{ and } -D_s\left(\frac{\partial C_S}{\partial r}\right)_{r=R_S} = \frac{j^{Li}}{a_s F} \tag{2}$$

where r represents the radial coordinate along the active particle, D_s is the mass diffusion coefficient of Li-ions in the electrolyte, R_S is the radius of the solid active particles, C_S is the concentration of lithium in the solid phase, and j^{Li} is the transmission current generated by the insertion of Li-ions at the electrolyte interface.

$$j^{Li} = a_s i_0 \begin{cases} a_{s,a} i_{n,a} \\ 0 \\ a_{s,c} i_{n,c} \end{cases} \text{ in the anode; separator and cathode} \tag{3}$$

2.3.2. Conservation of Momentum of Solid-Phase Charge. The equation of charge conservation in solid electrode materials follows ohm's law.[35,36]

$$\nabla(\sigma^{eff}\nabla\phi_s) - j^{Li} = 0 \tag{4}$$

in other words

$$\frac{\partial}{\partial x}\left(\sigma^{eff}\frac{\partial\phi_s}{\partial x}\right) = j^{Li} \tag{5}$$

with boundary conditions

$$-\sigma_-^{eff}\left(\frac{\partial\phi_s}{\partial x}\right)_{x=0} = \frac{1}{A} \text{ and } +\sigma_+^{eff}\left(\frac{\partial\phi_s}{\partial x}\right)_{x=L_z} = \frac{1}{A} \tag{6}$$

$$\left(\frac{\partial\phi_s}{\partial x}\right)_{x=l_n} = 0 \text{ and } \left(\frac{\partial\phi_s}{\partial x}\right)_{x=l_n+l_s} = 0 \tag{7}$$

where l_n is the length of the negative electrode, l_s is the length of the spacer, and l_p is the length of the positive electrode. The total length is denoted by $L_z = l_n + l_s + l_p$, which is calculated as the sum of l_n, l_s, and l_p. σ^{eff} is the effective conductivity of the solid phase. The symbols σ_+ and σ_- refer to the effective conductivities of the positive and negative electrodes. ϕ_+ and ϕ_- are the phase potentials of the positive and negative electrodes.

2.3.3. Conservation of Momentum in the Electrolyte Phase. The conservation of charge in electrolyte solution is expressed as[35,36]

$$\nabla(k^{eff}\nabla\phi_e) + \nabla(k_D^{eff}\nabla\ln C_e) + j^{Li} = 0 \tag{8}$$

in other words

$$\frac{\partial}{\partial x}\left(k^{eff}\frac{\partial\phi_e}{\partial x}\right) + \frac{\partial}{\partial x}\left(k_D^{eff}\frac{\partial\ln C_e}{\partial x}\right) = -j^{Li} \tag{9}$$

with boundary conditions

$$\left(\frac{\partial\phi_e}{\partial x}\right)_{x=0} = 0 \text{ and } \left(\frac{\partial\phi_e}{\partial x}\right)_{x=U} = 0 \tag{10}$$

where k^{eff} is the effective diffusive conductivity, known as the Bruggeman relation, given by $k^{eff} = k\varepsilon_e^{\beta}$, where β is the Bruggeman porosity index. k_D^{eff} is the effective ionic conductivity, given by

$$k_D^{eff} = \frac{2RTK^{eff}}{F}(t_+^0 - 1)\left(1 + \frac{\mathrm{d}\ln f_{\pm}}{\mathrm{d}\ln C_e}\right) \tag{11}$$

where $f_{\pm}$ is the molecular activity coefficient of the electrolyte, ε_e is the volume fraction of the electrolyte phase in the electrode, t_+^0 is the number of LFP transfers, R is the universal gas constant with a value of 8.3143 kJ/kg mol K, F is the Faraday constant with a value of 96,485 mol, and C_e is the concentration of lithium in the electrolyte phase.

2.3.4. Lithium Conservation in Electrolyte Phase. The liquid phase Li-ion equilibrium is described as follows[30]

$$\frac{\partial(\varepsilon_e c_e)C_S}{\partial t} - \nabla(D_e^{eff}\nabla c_e) - \frac{1 - t_+^0}{F}j^{Li} + \frac{i_e\nabla t_+}{F} = 0 \tag{12}$$

in other words[30]

$$\frac{\partial(\varepsilon_e c_e)C_S}{\partial t} = \frac{\partial}{\partial x}\left(D_e^{eff}\frac{\partial C_e}{\partial x}\right) + \frac{1 - t_+^0}{F}j^{Li} - \frac{i_e\nabla t_+}{F} \tag{13}$$

with boundary conditions

$$\left(\frac{\partial C_e}{\partial t}\right)_{x=0} = 0 \text{ and } \left(\frac{\partial C_e}{\partial x}\right)_{x=L} = 0 \tag{14}$$

where ε_e is the volume fraction or porosity of the electrolyte, D_e^{eff} is the effective diffusion coefficient (Bruggeman relation, $D_e^{eff} = D_e\varepsilon_e^{\beta}$), ε_s is the volume fraction of the solid particle in the electrode, ε_f is the volume fraction of the filler material in the electrode, and t_+^0 is the transfer number of Li^+ with respect to the velocity of the solvent (a function of electrolyte concentration, if assuming constant, $\frac{i_e\nabla t_+}{F} = 0$).

2.3.5. Electrochemical Kinetics at the Interface. The electrochemical reaction rate on the surface of electrode particles is usually governed by the Butler−Volmer equation;[37,38] the Butler−Volmer equation is used to couple a charge-species governing equation and is given by

$$j^{Li} = a_s i_0\left\{\exp\left[\frac{\alpha_a F}{RT}\eta\right] - \exp\left[\frac{\alpha_a F}{RT}\eta\right]\right\} \tag{15}$$

where local surface overpotential is given by the following formula[39]

$$\eta = \phi_s - \phi_e - U \tag{16}$$

The exchange current density is given by the following formula[39]

https://doi.org/10.1021/acsomega.3c08522
ACS Omega 2024, 9, 12753−12767

$$i_0 = k_m(C_e)^{\alpha_a}(C_{s,max} - C_{s,e})^{\alpha_a}(C_{s,e})^{\alpha_c} \quad (17)$$

where α_a is the transfer coefficient of the anode, α_c is the transfer coefficient of the cathode, α_s is the active surface area per electrode unit volume for electron transfer reactions (1/cm), ϕ_s is the phase potential for solid, ϕ_e is the electrolyte phase, $C_{s,max}$ is the maximum concentration of lithium in the solid phase, $C_{s,e}$ is the lithium concentration on the surface of solid particles, i_0 is the exchange current density (a function of lithium concentrations in both electrolyte and solid active materials), η is the overpotential (V), T is the temperature (K), and U is thermodynamics of the OCV.

2.3.6. Energy Equation. The energy balance equation is given by[35]

$$\nabla^2 T + \frac{q}{k} = \frac{1}{\alpha}\frac{\partial T}{\partial t} \quad (18)$$

in other words

$$\frac{\partial^2 T}{\partial x^2} + \frac{\partial^2 T}{\partial y^2} + \frac{\partial^2 T}{\partial z^2} + \frac{q}{k} = \frac{1}{\alpha}\frac{\partial T}{\partial t} \quad (19)$$

The above equation is further modified to

$$q = \frac{\partial(\rho C_p T)}{\partial t} - \nabla(k\nabla T) \quad (20)$$

also

$$\nabla(\sigma_+\nabla_{\phi_+}) = -j \quad (21)$$

$$\nabla(\sigma_-\nabla_{\phi_-}) = +j \quad (22)$$

$$q = (\sigma_+\nabla^2_{\phi_+}) + (\sigma_-\nabla^2_{\phi_-}) + q_{ECH} \quad (23)$$

where q_{ECH} is the electrochemical heat and is given by[35]

$$q_{ECH} = \frac{i_p(\phi_+ - \phi_-) + (\sigma_-\nabla^2_{\phi_-}) + \int_0^L j^{Li}\left(T_{ref}\frac{\partial U}{\partial t} - U_{ref}\right) dx}{L} \quad (24)$$

also

$$i_p = \int_0^{l_p} j^{Li}\, dx \quad (25)$$

$$j = -ai_p \quad (26)$$

where q is the heat generation rate during battery operation, which includes joule heating, electrochemical reaction heating, and entropic heating, ρ is the density, and C_p is the specific heat. The parameters used for the modeling are shown in Table 1.

2.4. Heat Source in the Electrochemical−Thermal Model. ANSYS FLUENT cannot simulate the heat generation in the reaction process, the heat source related to the electrochemical term of the battery is used in this paper.[43] The heat sources related to electrochemical terms in Li-ion batteries can be summarized into three main heat sources: electron ohmic heat source q_e, caused by internal contact resistance; ion ohmic heat sources q_i, caused by heat from the reaction current; and overpotentials q_r.

The electron ohmic heat source as in eq 27[43]

$$q_e = I^2\frac{R_c}{A} \quad (27)$$

where I is electronic current, A is the plane area of the electrode parallel to the current collector, and q_e is the internal contact resistance.

The reaction heat source is defined as in eq 28[43]

$$q_r = A\int_x^{x+dx} j^{Li}(\phi_s - \phi_e - U)\, dx \quad (28)$$

The ion ohmic heat source is defined as in eq 29[43]

$$q_i = A\int_x^{x+dx}\left[\delta^{eff}\left(\frac{\partial\phi_s}{\partial x}\right)^2 + k^{eff}\left(\frac{\partial\phi_e}{\partial x}\right)^2 + k_D^{eff}\left(\frac{\partial \ln c_e}{\partial x}\right)\left(\frac{\partial\phi_e}{\partial x}\right)\right]dx \quad (29)$$

Link it to the control equation in ANSYS FLUENT. The detailed parameters of LIB are shown in Table 1.

2.5. Orthotropic Thermal Conductivity of the Battery. According to the thermophysical principle of the lithium battery, the main parameters are made up of the specific heat capacity, density, and thermal conductivity. Considering that the internal parameters of lithium batteries change with the change in their working state, we start by consulting the technical manual and related literature. The internal parameters of the internal components of the lithium battery are shown in Table 2:[44]

In the simulation, it is necessary to account for the significant variations in thermodynamic parameters among different materials, which can increase the computational workload and simulation complexity. To address this, a weighted average calculation method is employed to determine the specific values for each material in the battery.

The density of the battery can be equivalent to the ratio of core mass to volume, as in eq 30

$$\rho = \frac{\sum_{i=1}^n \rho_i V_i}{\sum_{i=1}^n V_i} \quad (30)$$

where ρ_i and V_i are the material density and volume of each part of the battery core, respectively.

The specific heat capacity of the battery is weighted and averaged by the components of the battery, and the calculation, as in eq 31

$$C_P = \frac{1}{m}\sum_{i=1}^n C_i m_i \quad (31)$$

where m is the mass of the cell monomer; C_i is the specific heat capacity of the material inside the battery; m_i is the mass of i materials inside the battery.

The interior of a lithium battery is formed by stacking various materials, which integrate various materials in the battery into one substance.

The thermal conductivity of the Li-ion battery along the X, Y, and Z axes is calculated by the weighted calculation method.[45] The thermal conductivity in all directions is calculated, as in eq 32[45]

https://doi.org/10.1021/acsomega.3c08522
ACS Omega 2024, 9, 12753−12767

Table 4. Technical Specification of the $LiFePO_4$ Battery Cell

specification	value	unit
material for the electrolyte	carbonate based	
material for the anode	LiC_6	
material for the cathode	$LiFePO_4$	
voltage (nominal)	3.3	V
dimensions	185(h) × 135(w) × 26(t)	mm
capacity of the cell (nominal)	50	A h
discharge power	3367	W
energy (nominal)	160	W h
specific energy	114	W h/kg
energy density	247	W h/L
operating temperature	−30 to 55	°C
mass of the cell	1403	g
specific power	2400	W/kg
maximum discharge	500	A
internal resistance	0.36	mΩ
volume	0.649	L
storage temperature	−40 to 60	°C
number of cycles	min. 300, approximately 2000	cycles
maximum charge	500	A

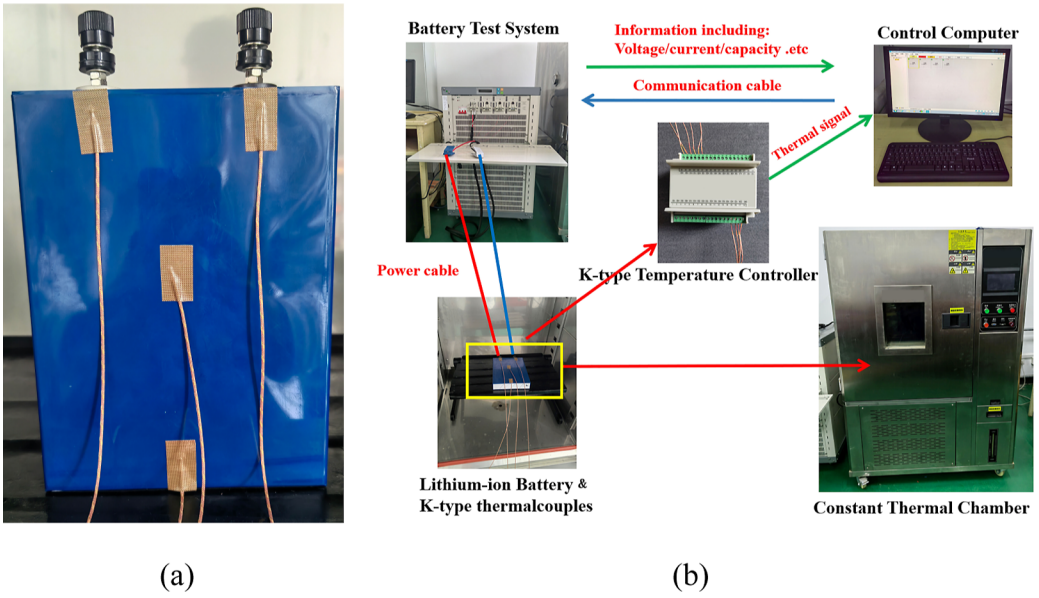

Figure 4. (a) Dimension of the battery and four locations of thermocouples; (b) demonstration of the test equipment.

$$\begin{cases} \lambda_x = \dfrac{l}{\sum_i \frac{dx_i}{\lambda_i}} = \dfrac{l}{\frac{dx_i}{\lambda_p}} + \dfrac{l}{\frac{dx_n}{\lambda_n}} + \dfrac{l}{\frac{dx_s}{\lambda_s}} \\ \lambda_y = \sum_i \dfrac{\lambda_i\, dy_i}{b} = \dfrac{\lambda_p\, dy_p + \lambda_n\, dy_n + \lambda_s\, dy_s}{h} \\ \lambda_z = \sum_i \dfrac{\lambda_i\, dz_i}{h} = \dfrac{\lambda_p\, dz_p + \lambda_n\, dz_n + \lambda_s\, dz_s}{h} \end{cases} \quad (32)$$

λ_x, λ_y, and λ_z are the thermal conductivity coefficients of the battery along the X, Y, and Z axes, respectively. x_i, y_i, and z_i are the layer thicknesses of i materials in the battery core. λ_p, λ_n, and λ_s are the thermal conductivity of the anode, cathode, and separator of the battery, respectively. l, b, and h are the stacking thicknesses of the batteries in the X, Y, and Z axis directions.

After the formula is weighted, the parameters of this type of battery are obtained and used in the battery setting, which are listed in Table 3.

3. EXPERIMENTAL SETUP AND NUMERICAL SIMULATION

3.1. Experimental Setup. The 3.2 V, 50 A h square shell lithium phosphate (LFP) battery is utilized as the subject of the experiment. The technical specifications of the batteries for this work are listed in Table 4.

Figure 4a illustrates the battery's dimensions and the placement of four thermocouples. Figure 4b describes the test equipment for the experiment. In the arrangement of K-type thermocouples placed on the surface of the battery, the battery is placed in the experimental thermostat set at a constant temperature of 253.15 K. The battery test system was used for battery charging and discharging experiments. Temperature

https://doi.org/10.1021/acsomega.3c08522
ACS Omega 2024, 9, 12753−12767

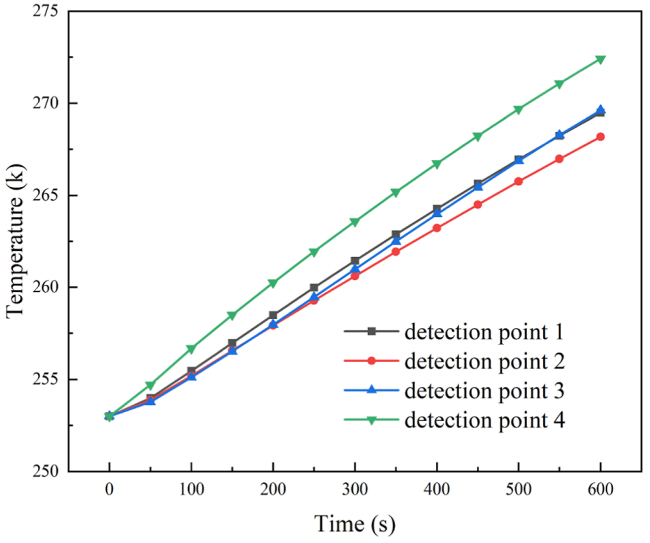

Figure 5. Temperature map of monitoring points at different locations on the battery surface.

testers are used to collect temperature information, and the voltage information collected by the test system is transmitted to the control computer to be saved. One of the thermocouples accuracy is 0.1 K. The uncertainties are mainly: thermocouple materials and manufacturing processes will directly affect its accuracy; the impact of the external environment may also have an impact on the accuracy of the thermocouple. First, the thermocouple's measuring terminals are made sure to be clean and free of oil or contaminants. After that, the thermocouple is fixed to the cell surface. The measuring terminals of the type-K thermocouple are fixed firmly to the cell surface. Four study points were selected on the front surface of the cell: point 1 directly below the N_Tab area, point 2 directly below the P_Tab area, point 3 in the center of the plane, and point 4 at the bottom of the plane to ensure that there is good thermal conduction contact with the surface of the cell. Finally, the thermocouples are connected to the data acquisition device to ensure a proper connection.

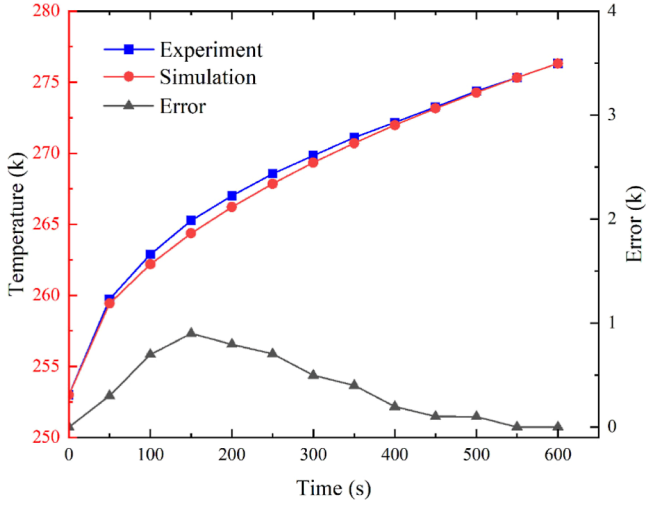

Figure 7. Comparative experiment between the fixed-frequency experiment and the simulation.

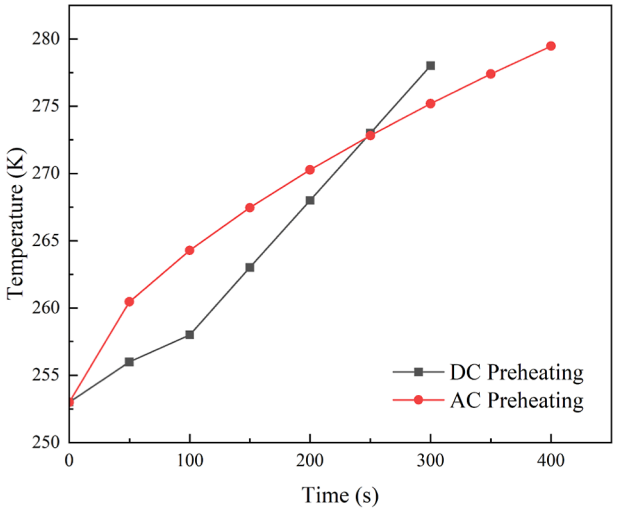

Figure 8. Comparison of temperature increases between DC heating and AC heating.

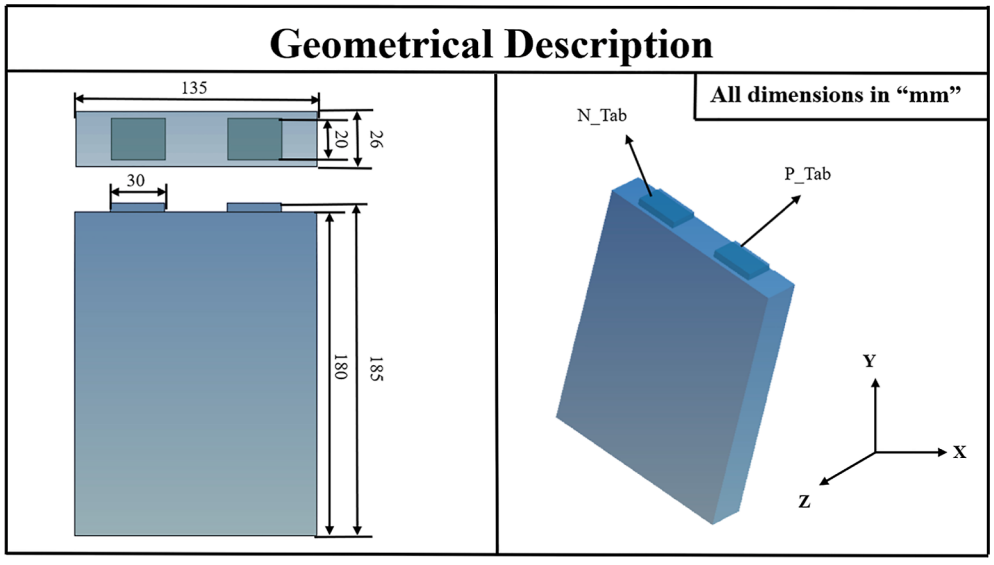

Figure 6. Battery modeling dimension diagram.

https://doi.org/10.1021/acsomega.3c08522
ACS Omega 2024, 9, 12753−12767

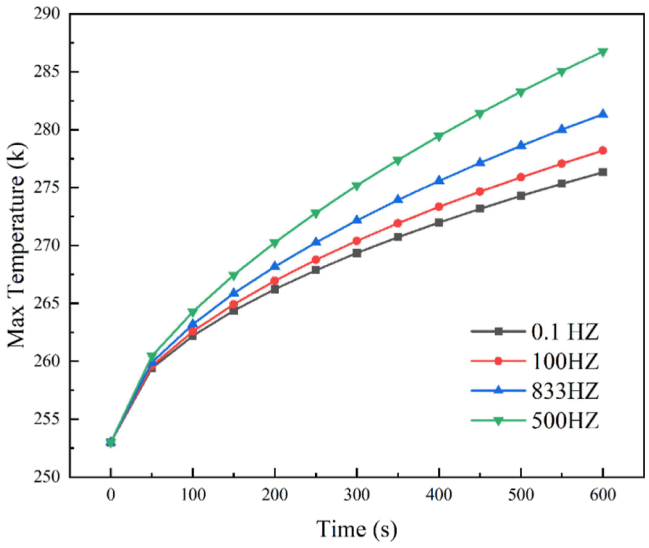

Figure 9. Comparison of different frequency amplitude heating of single cells.

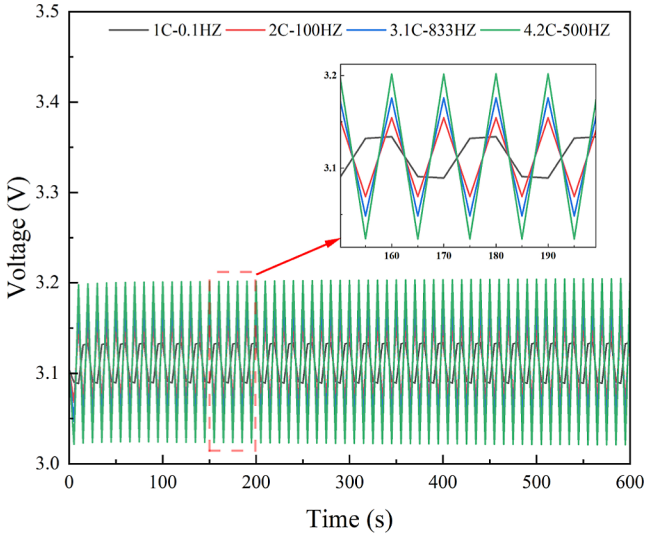

Figure 10. Variation of charging and discharging voltages of the battery at different AC frequencies.

Begin by recording the temperature change. Figure 5 shows the temperature increase at the four monitoring points at the 100 Hz-2C position. The ambient temperature was maintained at 253.15 K. The batteries were charged and discharged at 2C multiplier and 100 Hz through the battery test system, and the control computer recorded temperature samples from four locations. A constant temperature chamber ensures a stable test environment for the battery.

3.2. Numerical Simulation. For simulation modeling, the ANSYS FLUENT 2022R1 software was used for computational fluid dynamics (CFD) analysis. Inputs to the model: geometry and dimensions, material properties, electrochemical reactions, boundary conditions, thermal parameters, etc. Typical outputs of the model: potential distribution, current distribution, temperature distribution, electrochemical reaction rates, battery performance parameters, etc. These metrics provide insights into the electrochemical and thermal properties of the battery to optimize battery design and performance. The model solves physico-mathematical equations in heat transfer mechanisms using finite element techniques. The model solves physico-mathematical equations in heat transfer mechanisms using finite element techniques. The simulation of the high-frequency AC heating strategy is performed using the MSMD module. Figure 6 depicts the geometrical description of the battery model. The ANSYS fluent mesher is used to generate the finite volume mesh. The polyhedral mesh type can be used without affecting the quality of the output results, the minimum computational time required for the convergence of the solution is set to 0.72, the aspect ratio is 0.18, the mesh size of 2 mm is selected, the mesh generates a total of 145,158 nodes, and the average cell mass of the 223,121 cell mesh is 0.8321. The mesh reliability is high, and it meets the requirements of the simulation. The requirement of the Ansys fluent solver for mesh type is verified. The wall boundary value is set at 5 W/m^2 K for convective heat transfer. The established high-frequency heating strategy is verified, and the impact of low-temperature (253.15 K) preheating of the battery as well as the thermal distribution of battery temperature, voltage, SOC, and current density on battery aging are discussed. The heating strategy's correctness and effectiveness are confirmed.

3.3. Experiments Validation of Battery Heat Production Models. The preheating experiment is conducted using AC (0.1 Hz, 1C) with a fixed amplitude and frequency to preheat the battery at 253.15 K. Figure 7 displays the results of both the experiment and the simulation. The heating time is 600 s, and the simulation results are different from the experimental results. The differences can be attributed to the requirement of the P2D model to specify boundary conditions for accurately simulating heat exchange between the battery and its surrounding environment, including convection and radiation heat dissipation. The accuracy and response time of temperature sensors can lead to uncertainty in temperature measurements; the precision and stability of the power control of the heating equipment affect the heating process in the experiment and may lead to uneven or unstable temperature distribution; during experiments, thermal radiation and convective heat transfer may be affected by environmental conditions and equipment layout, thus introducing uncertainties; the chemical reactions and heat transfer processes within batteries are often very complex, and there may be uncertainties in modeling and understanding these processes. The P2D model may overlook some nonuniform reactions inside the battery. This somewhat affects the accuracy of the model, leading to discrepancies with actual measurements. The model has some local errors, the absolute temperature error is less than 1 K, indicating relative accuracy. At the conclusion of the preheating process, the simulation results align with the experimental results. The developed heat production model is validated and can be utilized to analyze the battery's low-temperature heating process.

3.4. Comparison and Verification with the DC Method. Wu et al.[46] proposed a DC heating strategy that utilizes variable frequency and variable amplitude to heat the battery from 253.15 to 258.15 K within 308 s. An electrothermal model was developed based on the electrochemical impedance spectra of LIB at varying temperatures. As shown in Figure 8, the temperature increase rate of AC electric heating is faster than that of DC electric heating before 262 s. Afterward, the temperature increase in C-rate of DC increased rapidly, reaching 278.15 K first. However, heating the battery with DC can lead to local overheating or uneven heating. Low-temperature heating can also cause lithium deposition, and frequent use of AC will affect the service life of batteries. The AC electric heating

https://doi.org/10.1021/acsomega.3c08522
ACS Omega 2024, 9, 12753−12767

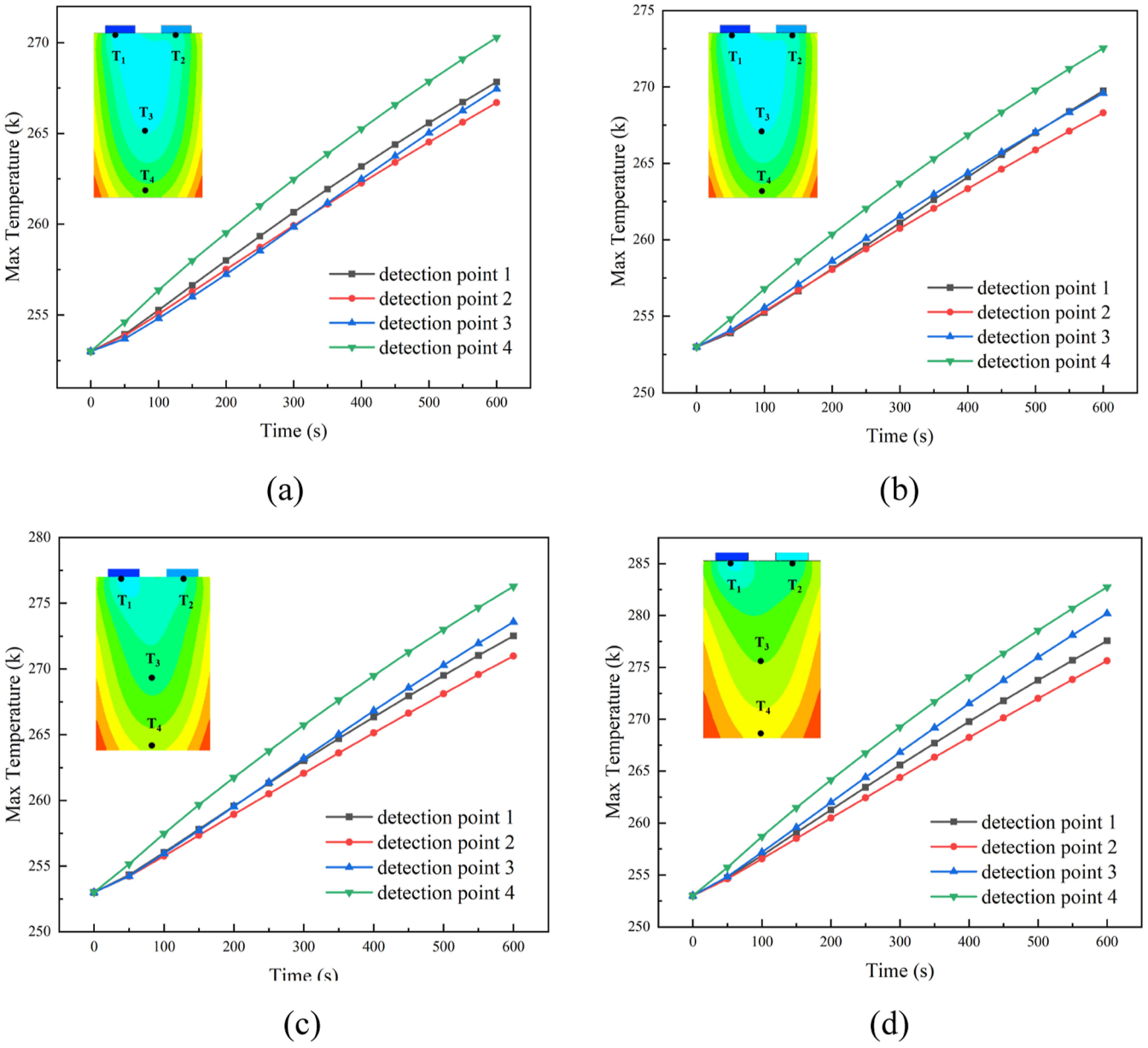

Figure 11. Battery monitoring point temperature under different charging and discharging frequencies. (a) 0.1 Hz-1C, (b) 100 Hz-2C, (c) 833 Hz-3.1C, and (d) 500 Hz-4.2C.

strategy is further validated to assess the influence of different frequencies and current rates on temperature rise and battery life.

4. RESULTS AND DISCUSSION

4.1. Influence of AC Frequency and Current Rate on Battery Temperature. This section examines the impact of the frequency and amplitude of AC on the heating effect of the battery. As shown in Figure 9, the state of charge (SOC) of the LIB is adjusted to 1 prior to heating, and the AC heating is conducted in an isothermal environment of 253.15 K. The study by Shang et al.[28] is referenced to determine the AC amplitude and frequency for the study; the frequency and amplitude are set at 0.1 Hz (1C), 100 Hz (2C), 500 Hz (4.2C), and 833 Hz (3.1C), respectively. When heated at 0.1, 100, 500, and 833 Hz for 600 s, the temperature rises by 16.1, 18.03, 21, and 26.86 K, respectively. It is observed that higher current amplitudes and frequencies result in a greater battery temperature rise rate. At 0.1 Hz, the battery cannot be preheated to 278.15 K. However, at frequencies of 100, 500, and 833 Hz, the battery reaches a temperature of 278.15 K at 595, 480, and 365 s respectively.

The voltage variation at different frequencies and amplitudes is also measured. At 0.1 Hz, the battery cannot be preheated to 278.15 K. However, at frequencies of 100, 500, and 833 Hz, the battery reaches a temperature of 278.15 K at 595, 480, and 365 s, respectively. As shown in Figure 10, at an amplitude of 4.2C, the AC instantaneous voltage can reach up to 3.2 V. At frequencies of 0.1, 10, 500, and 833 Hz, the voltage fluctuates between ranges of 3.088−3.131 V, 3.068−3.155 V, 3.021−3.205 V, and 3.047−3.178 V, respectively. Overall, the higher the frequency and amplitude, the greater the voltage variation becomes. The experimental LIB is known to have internal standard upper and lower voltage limits of 3.65 and 2.2 V, respectively; beyond these points, lithium precipitation may occur in the battery. Therefore,

https://doi.org/10.1021/acsomega.3c08522
ACS Omega 2024, 9, 12753−12767

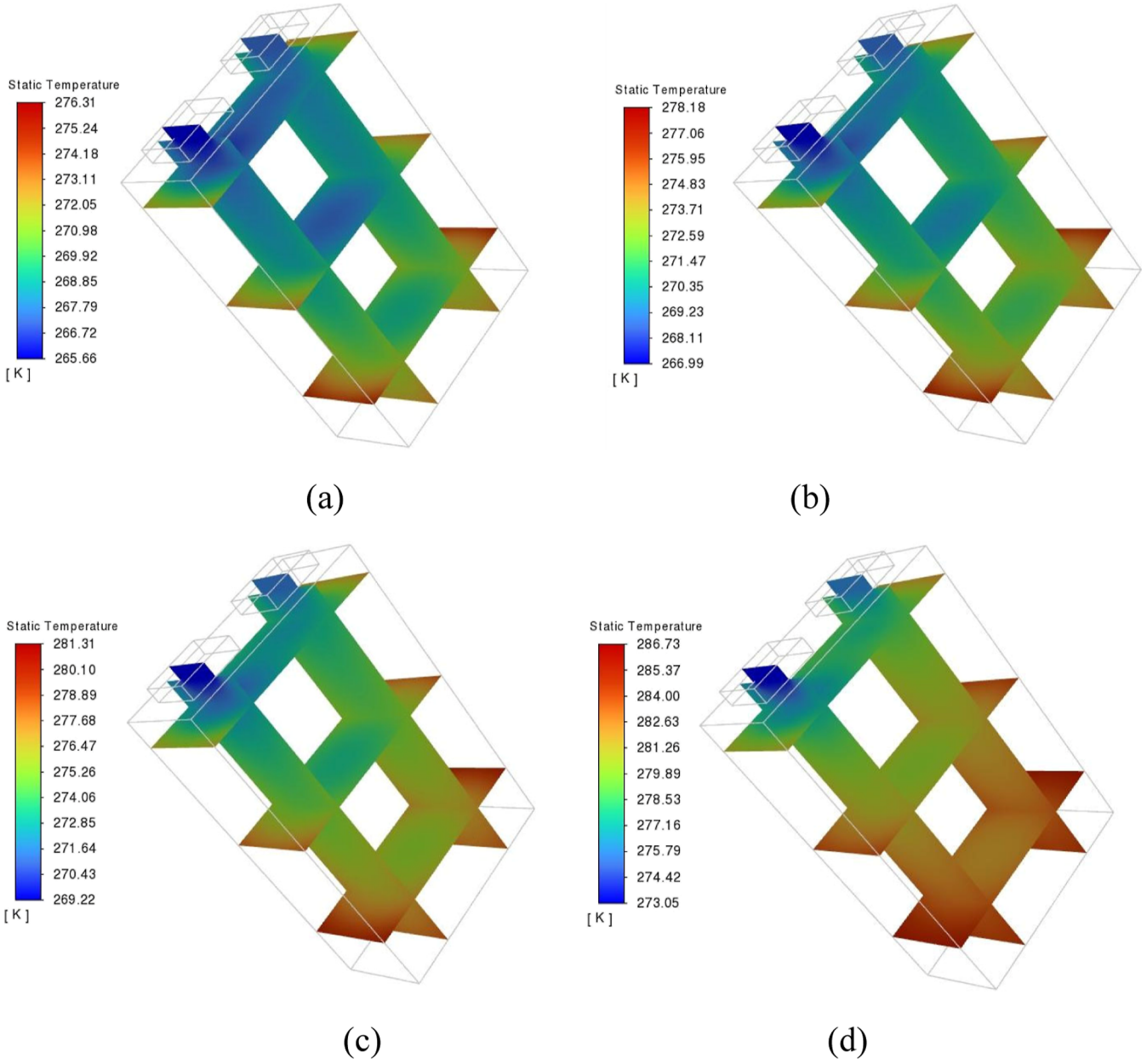

Figure 12. Temperature profile clouds at different charging and discharging frequencies. (a) 0.1 Hz-1C, (b) 100 Hz-2C, (c) 833 Hz-3.1C, and (d) 500 Hz-4.2C.

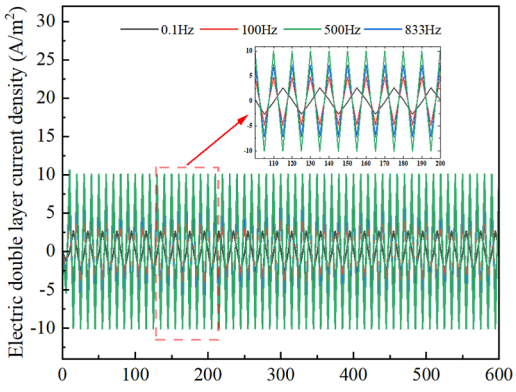

Figure 13. Variation of double layer current density on the surface of negative particles at different frequencies.

the choice of AC amplitude needs to be balanced between the heating rate and the risk of lithium precipitation.

Obtaining the real temperature field distribution of an LIB during charging or discharging is crucial. The temperature directly impacts the reaction rate inside the battery, with higher temperatures leading to faster reactions. Further promoting the temperature increase, a higher local temperature will destroy battery consistency. It may also lead to the occurrence of thermal runaway and cause safety accidents. In a low-temperature environment, the battery's temperature rise is uneven, exacerbating battery inconsistency and reducing battery life. By monitoring the internal temperature distribution and changes in the battery, we can more accurately analyze its electrochemical performance. As shown in Figure 11, four research points were selected: point 1 in the N_Tab region, point 2 in the P_Tab region, point 3 at the plane center, and point 4 at the plane bottom. The experimental temperature is set

https://doi.org/10.1021/acsomega.3c08522
ACS Omega 2024, 9, 12753−12767

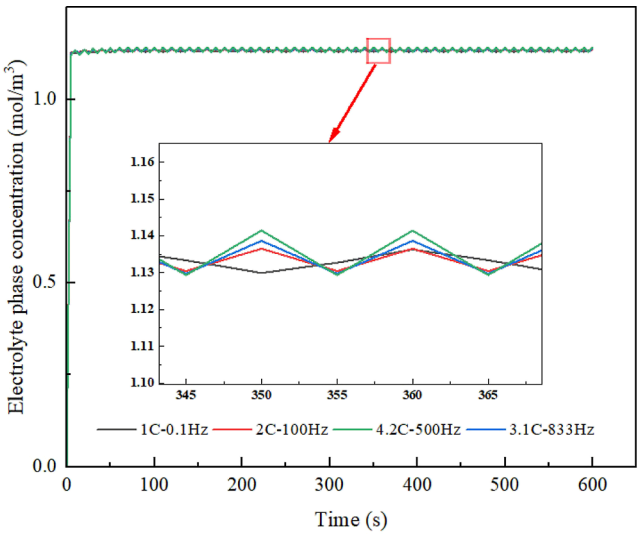

Figure 14. Variation curve of electrolyte phase concentration with time at different frequencies.

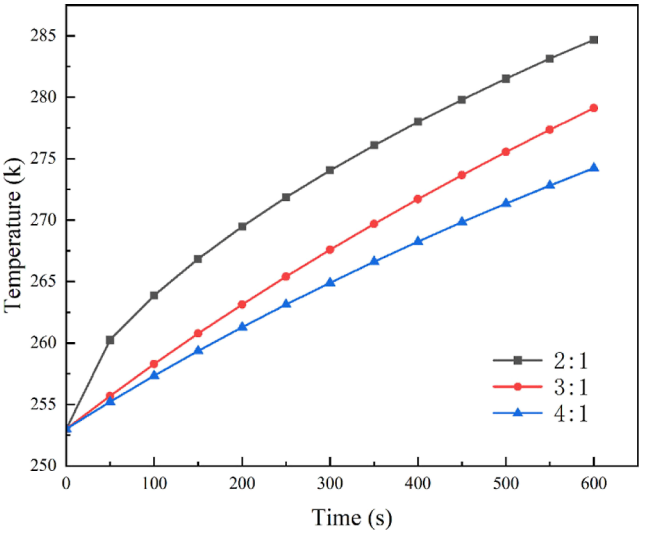

Figure 15. Image of different proportion temperature rises of the 500HZ frequency AB battery pack.

at 253.15 K, and the heating is performed using AC at different frequencies of 0.1 Hz (1C), 100 Hz (2C), 833 Hz (3.1C), and 500 Hz (4.2C). Monitoring the internal temperature distribution and change of the battery, the bottom temperature of the single cell temperature field distribution is obviously higher than that of the Tab part, and the temperature difference between positive and negative areas is not obvious. Only ohmic heat generation is observed in the simulation of the positive and negative ear regions. The temperature in the N_Tab region is higher than that in the P_Tab region. The cells were heated for 600 s at the frequencies of 0.1 Hz (1C), 100 Hz (2C), 833 Hz (3.1C), and 500 Hz (4.2C). The maximum errors at battery monitoring points are 3.596, 4.23, 5.29, and 7.11 K, respectively. The closer a battery is to the middle, the higher its bottom temperature becomes. Additionally, a higher frequency results in a greater rate of temperature rise in the battery.

According to the thermal distribution cloud chart, the device was charged or discharging. The bottom temperature of the single battery's internal temperature field distribution is significantly higher than that of the Tab part. As shown in Figure 12, the temperature at the bottom of the battery gradually decreases from the temperatures at the N_Tab and P_Tab. The temperature difference between the positive and negative regions is not substantial. The temperature difference between the positive and negative regions is not significant. There is a noticeable temperature difference between batteries and a single battery. The temperature inside the battery is lower in the middle and gradually increases toward the sides. The temperature rises gradually from the inside to the outside.

4.2. Effect of AC Frequency on Battery Life. The heating effect suggests that selecting a higher AC frequency can heat the battery faster. This is crucial for studying the effects of high-frequency charging or discharging at low temperatures (253.15 K) on lithium precipitation in the battery. By combining with the model, the electrochemical performance of the battery at different frequencies is analyzed. When positive and negative alternating currents are applied, the double electric layer on the surface of the positive and negative active material particles significantly influences the battery's internal electrochemistry. To compare the current density of the double electric layer on the surface of the negative active material particles at different frequencies, it is important to understand that the double electric layer on the surface of both positive and negative active material particles has a significant impact on the internal electrochemical reaction of the battery. As shown in Figure 13, by analysis of the magnitude of the *y*-axis double layer current density on the surface of the anode active material particles under different frequency heating, the higher current density through the double layer corresponds to a larger double layer potential. The bilayer influences the speed of the electrode reaction; a higher bilayer potential leads to a faster electron transfer rate. Therefore, a higher current density on the surface of anode particles participating in the Li-ion embedding reaction helps prevent lithium precipitation at the battery's anode.

The concentration of the electrolyte can influence the migration rate of Li-ions in the battery. As shown in Figure 14, a higher electrolyte concentration can improve the migration rate of Li-ions, thereby reducing the battery's internal resistance and extending its lifespan. However, an excessive electrolyte concentration may result in an overdeposition of Li-ions on the negative electrode, leading to the formation of lithium dendrites. This could cause a short circuit or loss of battery capacity, ultimately shortening the battery's life. Furthermore, an overly high electrolyte concentration might decrease the solubility of Li-ions, leading to an increase in Li-ion loss during charging or discharging. This reduces the active materials available for the battery and shortens its lifespan.

The optimal electrolyte concentration for a lithium iron phosphate battery is between 1.0 and 1.3 mol/L, and the electrolyte concentration in this range provides sufficient Li-ion transmission rate and better battery performance while maintaining high safety. The experimental temperature is set to 253.12 K, and simulations were conducted at different frequencies: 0.1 Hz (1C), 100 Hz (2C), 833 Hz (3.1C), and 500 Hz (4.2C); the electrolyte concentration increases with frequency. At 0.1, 100, 833, and 500 Hz, the electrolyte concentrations are 1.1262−1.363 mol/L, 1.1266−1.366 mol/L, 1.124−1.1388 mol/L, and 1.121 mol/L, respectively. These electrolyte concentrations fall within the appropriate range and will not affect the battery's lifespan.

4.3. Effect of the Different AB Batteries Ratio on Temperature Rise. According to the AB battery circuit, a high

https://doi.org/10.1021/acsomega.3c08522
ACS Omega 2024, 9, 12753−12767

and low potential difference must be generated for the circuit to function properly. The single-cell simulation test shows that the frequency and amplitude of the battery at 500 Hz meet the design requirements. At that frequency, the AB battery was simulated at ratios of 2:1, 3:1, and 4:1. To conduct the AC heating simulation, the initial SOC of the LIB is set to 1. The simulation is carried out in a 253.12 K isothermal environment with ratios of 2:1, 3:1, and 4:1 for the AB battery pack.

As shown in Figure 15, the battery temperature rise image was obtained under various ratios of the AB batteries. The temperature rise rate increases with greater current amplitude and frequency. At a frequency of 500 Hz, for the ratios of 2:1 and 3:1, the module reaches a temperature of 278.15 K in 405 and 568 s respectively. However, when the ratio is 4:1, the temperature fails to reach 278.15 K within 600 s.

5. CONCLUSIONS

In this study, a high-frequency alternating current (AC) heating strategy was designed without the need for external heating equipment or an additional power supply. Using the P2D model in ANSYS, the battery heating performance and internal and external heat distribution are simulated and predicted, and the effectiveness of the model is demonstrated by examples. The proposed AC heating strategy can change the heating rate of the lithium-ion battery by changing the switching frequency, and the optimal heating effect is achieved at a frequency of 500 Hz (4.2C), which heats up the test battery from 253.15 to 273.15 K in 365 s, with an average heating rate of 3.29 K/min, and the temperature distribution of the battery is consistent. The proposed heating strategy and frequency have been proven to be harmless to the health of the battery. The AC heating method of the power battery can improve the battery performance, such as charging and discharging efficiency, and realize rapid heating, so it has important application value.

AUTHOR INFORMATION

Corresponding Author

Yuan Li − *College of Energy and Power Engineering, Inner Mongolia University of Technology, Hohhot, Inner Mongolia 010051, China;* orcid.org/0000-0003-0960-4815; Email: yuanli@imut.edu.cn

Authors

Wei Cui − *College of Energy and Power Engineering, Inner Mongolia University of Technology, Hohhot, Inner Mongolia 010051, China*

Ze-yu Ma − *College of Energy and Power Engineering, Inner Mongolia University of Technology, Hohhot, Inner Mongolia 010051, China*

Jing-xuan Nie − *College of Energy and Power Engineering, Inner Mongolia University of Technology, Hohhot, Inner Mongolia 010051, China*

Yu-chen Liu − *College of Energy and Power Engineering, Inner Mongolia University of Technology, Hohhot, Inner Mongolia 010051, China*

Complete contact information is available at: https://pubs.acs.org/10.1021/acsomega.3c08522

Notes

The authors declare no competing financial interest.

ACKNOWLEDGMENTS

This work was supported by the scientific research project of universities in the Inner Mongolia Autonomous Region with grant no. [NJZZ22373], Major demonstration projects of scientific and technological innovation project of Inner Mongolia Autonomous Region with grant No. [2023JBGS0005], Central government guides local science and technology development program with grant No. [2022ZY0113], the Program for Young Talents of Science and Technology in Universities of Inner Mongolia Autonomous Region with grant no. [NJYT24013], the basic research expenses of universities directly under the Inner Mongolia Autonomous Region with grant no. [JY20220117], and the scientific research project of Inner Mongolia University of Technology with grant no. [ZZ202120].

NOMENCLATURE

A	area [m^2]
C_p	specific heat capacity [J/(kg·K)]
C_e	concentration of lithium in the electrolyte phase [mol/m^3]
C_s	concentration of lithium in the solid phase [mol/m^3]
$C_{p,i}$	specific heat [J/(kg·K)]
R_s	radius of a solid active material particle [mm]
ε_1	volume fraction for the solid phase
ε_2	volume fraction for the liquid phase
C_0	initial electrolyte Li^+ concentration[mol/m^3]
C_1	initial solid Li^+ concentration for the electrode [mol/m^3]
$C_{1,max}$	maximum solid Li^+ concentration for the electrode [mol/m^3]
$D_{s,i}$	reference diffusivity for the electrode [m^2/s]
D_s	mass diffusion coefficient of lithium-ion in the electrolyte
E_d	activation energy that controls the temperature sensitivity of D_s [kJ/mol]
δ_i	conductivity for the electrode [S/m]
k	ionic conductivity of the electrolyte [S/m]
D_e^{eff}	effective diffusion coefficient
t_+	transport number of lithium-ions
γ	Bruggeman correction factor
R	universal gas constant [8.3143 kJ/kg mol K]
F	Faraday's constant [96,485 C/mol]
j^{Li}	transfer current resulting from lithium insertion at the electrode interface [A/m^2]
q	heat generation rate [W]
U	electrode potential of the reaction or thermodynamic open circuit potential [V]
V	cell voltage or cell potential [V]
T	absolute temperature [K]
l_n	length of the negative electrode [mm]
l_s	length of the separator [mm]
l_p	length of the positive electrode [mm]
L_z	overall length ($L_z = l_n + l_s + l_p$ [mm])

ACRONYMS

DC	direct current
AC	alternating current
C-rate	charge/discharge rate
BTMS	battery thermal management system
Li-ion	lithium ion
SOC	state of charge
P2D	pseudo two-dimensional
LIB	lithium-ion battery

https://doi.org/10.1021/acsomega.3c08522
ACS Omega 2024, 9, 12753−12767

HEV	hybrid electric vehicle
EV	electric vehicle
MSMD	multi scale multi domain
LFP	lithium phosphate

GREEK SYMBOLS

α	thermal diffusivity [m^2/s]
β	Burggeman porosity exponent
ρ	density [kg/m^3]
$\mathcal{T}_i$	volume fraction of the electrolyte phase
α_a	transfer coefficient of the anode
α_c	transfer coefficient of the cathode
∇	gradient operator
ϕ_s	solid phase potential [V]
ϕ_e	electrolyte phase potential [V]

SUBSCRIPTS

∞	ambient
0	initial
p	positive electrode
n	negative electrode
a	anode
c	cathode
e	electrolyte
f	filler
exp	experimental
eff	effective
Li	lithium
x, y, z	Cartesian coordinate directions

REFERENCES

(1) Wang, J.; Li, Y.; Liu, X.; Shen, C.; Zhang, H.; Xiong, K. Recent active thermal management technologies for the development of energy-optimized aerospace vehicles in China. *Chin. J. Aeronaut.* **2021**, *34*, 1−27.

(2) Teixeira, A. C. R.; Sodré, J. R. Impacts of replacement of engine powered vehicles by electric vehicles on energy consumption and CO 2 emissions. *Transp. Res. D: Transp. Environ.* **2018**, *59*, 375−384.

(3) Hu, X.; Zou, C.; Zhang, C.; Li, Y. Technological Developments in Batteries: A Survey of Principal Roles, Types, and Management Needs. *IEEE Power Energy Mag.* **2017**, *15*, 20−31.

(4) Talele, V.; Thorat, P.; Gokhale, Y. P.; Vk, M. Phase change material based passive battery thermal management system to predict delay effect. *J. Energy Storage* **2021**, *44*, 103482.

(5) Jilte, R.; Afzal, A.; Panchal, S. A novel battery thermal management system using nano-enhanced phase change materials. *Energy* **2021**, *219*, 119564.

(6) Mevawalla, A.; Panchal, S.; Tran, M. K.; Fowler, M.; Fraser, R. One dimensional fast computational partial differential model for heat transfer in lithium-ion batteries. *J. Energy Storage* **2021**, *37*, 102471.

(7) Yang, R.; et al. Comparative Study on the Thermal Characteristics of Solid-state Lithium-ion Batteries. *IEEE Trans. Transp. Electrif.* **2023**, 1.

(8) Li, Y.; Guo, H.; Qi, F.; Guo, Z.; Li, M. Comparative Study of the Influence of Open Circuit Voltage Tests on State of Charge Online Estimation for Lithium-Ion Batteries. *IEEE Access* **2020**, *8*, 17535−17547.

(9) Senyshyn, A.; Mühlbauer, M.; Dolotko, O.; Ehrenberg, H. Low-temperature performance of Li-ion batteries: The behavior of lithiated graphite. *J. Power Sources* **2015**, *282*, 235−240.

(10) Wu, S.; Xiong, R.; Li, H.; Nian, V.; Ma, S. The state of the art on preheating lithium-ion batteries in cold weather. *J. Energy Storage* **2020**, *27*, 101059.

(11) Talele, V.; Moralı, U.; Patil, M. S.; Panchal, S.; Mathew, K. Optimal battery preheating in critical subzero ambient condition using different preheating arrangement and advance pyro linear thermal insulation. *Therm. Sci. Eng. Prog.* **2023**, *42*, 101908.

(12) Singh, L. K.; Kumar, R.; Gupta, A. K.; Sharma, A. K.; Panchal, S. Computational study on hybrid air-PCM cooling inside lithium-ion battery packs with varying number of cells. *J. Energy Storage* **2023**, *67*, 107649.

(13) Wang, Y.; Zhang, X.; Chen, Z. Low temperature preheating techniques for Lithium-ion batteries: Recent advances and future challenges. *Appl. Energy* **2022**, *313*, 118832.

(14) Qin, P.; Sun, J.; Yang, X.; Wang, Q. Battery thermal management system based on the forced-air convection: A review. *Etransportation* **2021**, *7*, 100097.

(15) Joshi, A. K.; Kakati, P.; Dandotiya, D.; Soundra Pandiyan, P.; Patil, N. G.; Panchal, S. Computational analysis of preheating cylindrical lithium-ion batteries with fin-assisted phase change material. *Int. J. Mod. Phys. C* **2023**, 2450047.

(16) Bais, A.; Subhedar, D.; Panchal, S. Experimental investigation of longevity and temperature of a lithium-ion battery cell using phase change material based battery thermal management system. *Mater. Today: Proc.* **2023**.

(17) Kausthubharam; Koorata, P. K.; Panchal, S. Thermal management of large-sized LiFePO4 pouch cell using simplified mini-channel cold plates. *Appl. Therm. Eng.* **2023**, *234*, 121286.

(18) Wu, S.; Xiong, R.; Li, H.; Nian, V.; Ma, S. The state of the art on preheating lithium-ion batteries in cold weather. *J. Energy Storage* **2020**, *27*, 101059.

(19) Shang, Y.; Zhu, C.; Lu, G.; Zhang, Q.; Cui, N.; Zhang, C. Modeling and analysis of high-frequency alternating-current heating for lithium-ion batteries under low-temperature operations. *J. Power Sources* **2020**, *450*, 227435.

(20) Ruan, H.; Jiang, J.; Sun, B.; Su, X.; He, X.; Zhao, K. An optimal internal-heating strategy for lithium-ion batteries at low temperature considering both heating time and lifetime reduction. *Appl. Energy* **2019**, *256*, 113797.

(21) Wu, X.; Cui, Z.; Chen, E.; Du, J. Capacity degradation minimization oriented optimization for the pulse preheating of lithium-ion batteries under low temperature. *J. Energy Storage* **2020**, *31*, 101746.

(22) Chen, J., et al. A Convolutional Neural Network for Estimation of Lithium-Ion Battery State-of-Health during Constant Current Operation. *2023 IEEE Transportation Electrification Conference & Expo (ITEC)*, 2023; pp 1−6.

(23) Cai, F.; Chang, H.; Yang, Z.; Duan, C.; Tu, Z. A rapid self-heating strategy of lithium-ion battery at low temperatures based on bidirectional pulse current without external power. *J. Power Sources* **2022**, *549*, 232138.

(24) Zhang, Y.; Yang, Y.; Shang, Y.; Cui, N. A high frequency AC heater based on switched capacitors for lithium-ion batteries at low temperature. *J. Energy Storage* **2021**, *42*, 102977.

(25) Zhang, J.; Ge, H.; Li, Z.; Ding, Z. Internal heating of lithium-ion batteries using alternating current based on the heat generation model in frequency domain. *J. Power Sources* **2015**, *273*, 1030−1037.

(26) Hu, Z.; Liu, F.; Chen, P.; Xie, C.; Huang, M.; Hu, S.; Lu, S. Experimental study on the mechanism of frequency-dependent heat in AC preheating of lithium-ion battery at low temperature. *Appl. Therm. Eng.* **2022**, *214*, 118860.

(27) Jiang, J.; Ruan, H.; Sun, B.; Wang, L.; Gao, W.; Zhang, W. A low-temperature internal heating strategy without lifetime reduction for large-size automotive lithium-ion battery pack. *Appl. Energy* **2018**, *230*, 257−266.

(28) Shang, Y.; Xia, B.; Cui, N.; Zhang, C.; Mi, C. C. An Automotive Onboard AC Heater Without External Power Supplies for Lithium-Ion Batteries at Low Temperatures. *IEEE Trans. Power Electron.* **2018**, *33*, 7759−7769.

(29) Doyle, M.; Fuller, T. F.; Newman, J. Modeling of galvanostatic charge and discharge of the lithium/polymer/insertion cell. *J. Electrochem. Soc.* **1993**, *140*, 1526−1533.

(30) Panchal, S.; Dincer, I.; Agelin-Chaab, M.; Fraser, R.; Fowler, M. Transient electrochemical heat transfer modeling and experimental

https://doi.org/10.1021/acsomega.3c08522
ACS Omega 2024, 9, 12753−12767

validation of a large sized LiFePO4/graphite battery. *Int. J. Heat Mass Transfer* **2017**, *109*, 1239−1251.
(31) Xu, M.; Zhang, Z.; Wang, X.; Jia, L.; Yang, L. A pseudo three-dimensional electrochemical-thermal model of a prismatic LiFePO 4 battery during discharge process. *Energy* **2015**, *80*, 303−317.
(32) He, C. X.; Yue, Q. L.; Wu, M. C.; Chen, Q.; Zhao, T. S. A 3D electrochemical-thermal coupled model for electrochemical and thermal analysis of pouch-type lithium-ion batteries. *Int. J. Heat Mass Transfer* **2021**, *181*, 121855.
(33) Fragiacomo, P.; Astorino, E.; Chippari, G.; De Lorenzo, G.; Czarnetzki, W. T.; Schneider, W. Dynamic modeling of a hybrid electric system based on an anion exchange membrane fuel cell. *Cogent Eng.* **2017**, *4*, 1357891.
(34) Yang, N.; Zhang, X.; Li, G.; Hua, D. Assessment of the forced air-cooling performance for cylindrical lithium-ion battery packs: A comparative analysis between aligned and staggered cell arrangements. *Appl. Therm. Eng.* **2015**, *80*, 55−65.
(35) Li, G.; Li, S. Physics-Based CFD Simulation of Lithium-Ion Battery under the FUDS Driving Cycle. *ECS Trans.* **2015**, *64*, 1−14.
(36) Lu, L.; Han, X.; Li, J.; Hua, J.; Ouyang, M. A review on theKey issues for lithium-ion battery management in electric vehicles. *J. Power Sources* **2013**, *226*, 272−288.
(37) Fotouhi, A.; Auger, D. J.; Propp, K.; Longo, S.; Wild, M. A review on electric vehicle battery modelling: From Lithium-ion toward Lithium-Sulphur. *Renew. Sustain. Energy Rev.* **2016**, *56*, 1008−1021.
(38) Huo, W.; He, H.; Sun, F. Electrochemical-thermal modeling for a ternary lithium ion battery during discharging and driving cycle testing. *RSC Adv.* **2015**, *5*, 57599−57607.
(39) Huo, Y.; Rao, Z.; Liu, X.; Zhao, J. Investigation of power battery thermal management by using mini-channel cold plate. *Energy Convers. Manage.* **2015**, *89*, 387−395.
(40) Huang, Y.; Lai, H. Effects of discharge rate on electrochemical and thermal characteristics of LiFePO4/graphite battery. *Appl. Therm. Eng.* **2019**, *157*, 113744.
(41) Xu, M.; Zhang, Z.; Wang, X.; Jia, L.; Yang, L. A pseudo three-dimensional electrochemical-thermal model of a prismatic LiFePO 4 battery during discharge process. *Energy* **2015**, *80*, 303−317.
(42) An, Z.; Jia, L.; Wei, L.; Dang, C.; Peng, Q. Investigation on lithium-ion battery electrochemical and thermal characteristic based on electrochemical-thermal coupled model. *Appl. Therm. Eng.* **2018**, *137*, 792−807.
(43) Li, Y.; Qi, F.; Guo, H.; Guo, Z.; Li, M.; Wu, W. Characteristic investigation of an electrochemical-thermal coupled model for a LiFePO4/Graphene hybrid cathode lithium-ion battery. *Case Stud. Therm. Eng.* **2019**, *13*, 100387.
(44) Spotnitz, R.; Franklin, J. Abuse behavior of high-power, lithium-ion cells. *J. Power Sources* **2003**, *113*, 81−100.
(45) Guo, G.; Long, B.; Cheng, B.; Zhou, S.; Xu, P.; Cao, B. Three-dimensional thermal finite element modeling of lithium-ion battery in thermal abuse application. *J. Power Sources* **2010**, *195*, 2393−2398.
(46) Wu, X.; Cui, Z.; Chen, E.; Du, J. Capacity degradation minimization oriented optimization for the pulse preheating of lithium-ion batteries under low temperature. *J. Energy Storage* **2020**, *31*, 101746.

https://doi.org/10.1021/acsomega.3c08522
ACS Omega 2024, 9, 12753−12767